Expanding Geothermal Energy Utilization through a New Solid-State Thermoelectric Power Generator

Ziming Jing[1], Kirk Nuzum[2] and Mukul M. Sharma[1]
University of Texas at Austin [1], Geothermix[2]
ziming.jing@utexas.edu

Keywords: Thermoelectric Generator; Waste-heat Recovery; Solid-state Energy Conversion; Parasitic Load reduction; System integration

ABSTRACT

Commercial geothermal power plants typically operate at thermal to electric conversion efficiencies of ~10-18%, constrained by parasitic loads and system level losses. This work presents a solid-state thermoelectric power generation system that recovers geothermal waste heat by directly converting thermal energy into electricity via the Seebeck effect. Operating without moving parts, the system offers a compact, reliable, and near maintenance free solution that is readily retrofittable to turbine exhausts, separator units, wellhead facilities, and heat rejection stages, where low to medium temperature thermal energy is routinely discharged in geothermal and other industrial processes. A field deployable thermoelectric power cell was designed, fabricated, and experimentally evaluated under laboratory thermal conditions, producing ~228 W from a scaled down 4-module Mk III configuration at a temperature difference of ~71 °C, corresponding to a projected output of ~1.02 kW for a fully populated 16-module stack. Building on this experimentally validated scaling behavior, the upgraded Mk IV architecture is projected to deliver ~10 kW using 16-module at a temperature difference of 220 °C under field conditions, with conversion efficiencies ranging from ~0.83% to 3.88% over the evaluated operating range of 50-225 °C.

1. INTRODUCTION

Geothermal energy is a mature renewable resource capable of providing continuous baseload power with a high capacity factor, independent of weather conditions and time of day variability (DiPippo, 2016; Lund et al., 2022). Commercial geothermal power plants primarily rely on dry steam, flash steam, and binary cycle configurations, in which subsurface thermal energy is first converted into mechanical work and subsequently into electricity (Bertani, 2015). Although these technologies are well established, their thermal to electric conversion efficiencies typically remain in the range of ~10-18%, limited by parasitic loads, thermodynamic irreversibility, and the performance constraints of turbines, heat exchangers, and working fluids (Liu et al., 2024; Zarrouk & Moon, 2014). Consequently, a substantial fraction of geothermal heat remains unutilized and is discharged to the environment, especially low and medium temperature thermal energy around 50-250 °C, from separator units, wellhead facilities, and heat rejection stages (Nath et al., 2024; Rybach & Kohl, 2004). Higher quality heat with temperatures from 250 °C to 800 °C is available from turbine exhaust, flue gas, steam generators and as a combustion byproduct from heaters.

These losses are especially significant in geothermal systems operating outside high enthalpy reservoirs, including flash steam tail brine, binary plant reinjection streams, and enhanced geothermal systems. In such cases, conventional thermodynamic cycles such as Organic Rankine Cycle and Kalina systems become increasingly complex, capital intensive, and less efficient as source temperatures decrease (Liu et al., 2024; X. Zhang et al., 2012). This has led to growing interest in energy conversion technologies that can directly recover electricity from medium and low-grade geothermal heat.

Thermoelectric generators provide a fundamentally different pathway for geothermal power conversion by directly transforming temperature gradients into electrical energy through the Seebeck effect (Q. Zhang et al., 2022). As solid-state devices, thermoelectric conversion modules operate without turbines, compressors, or phase change working fluids, enabling compact system architectures with high reliability and minimal maintenance requirements (Bell, 2008; Hao et al., 2016). These characteristics make thermoelectric systems well suited for geothermal environments where continuous operation, mechanical robustness, and long-term stability are essential. Moreover, thermoelectric generators can be deployed in modular and distributed configurations, enabling retrofit integration with existing geothermal infrastructure to recover thermal energy from heat streams that are unsuitable for conventional power cycles.

Despite these advantages, large scale implementation of thermoelectric power generation in geothermal applications remains limited. The primary challenges arise from lower conversion efficiency, complexity of the thermoelectric module to module interconnections across large modular assemblies, which often exhibit low tolerance to individual component failure. These challenges are further compounded by system level constraints related to heat exchange performance, thermal uniformity, and the design complexity of scalable flow distribution architectures (Li et al., 2021; Luo et al., 2024; Wang et al., 2025;

Xie et al., 2023). In response, previous studies have primarily reported laboratory scale thermoelectric systems for geothermal and waste heat recovery, together with numerical and analytical investigations of downhole and surface mounted configurations. While these efforts have significantly advanced understanding of thermoelectric performance and economic feasibility, most reported demonstrations remain limited to relatively small power outputs, simplified boundary conditions, or short-duration testing, underscoring the need for further investigation of long term reliability and practical field deploy ability.

A clear need exists for scalable, industrial-grade thermoelectric systems capable of sustained kilowatt to megawatt scale power generation using modular architectures compatible with surface geothermal infrastructure. Achieving such performance requires maintaining stable thermal gradients across large thermoelectric stacks while minimizing parasitic thermal losses, ensuring uniform fluid distribution, and preserving reliable electrical operation under repeated thermal cycling.

A field deployable solid-state thermoelectric power generation system is presented for geothermal waste heat recovery, with adaptability to a broader range of industrial surface heat recovery applications. The system employs a modular, plate-based architecture that enables scalable power output while maintaining a compact form factor and favorable thermal uniformity. A complete thermoelectric generator was designed, fabricated, and experimentally evaluated under simulated geothermal conditions in the laboratory. A compact, scaled down 4-module configuration produced ~228 W at a temperature difference of 71 °C, corresponding to a projected output of 1.02 kW for a fully populated 16-module stack. Experimental results further indicate that electrical power output increases rapidly with the applied temperature difference, supporting extension of a single power cell to multi-kilowatt output levels, with projected power generation on the order of 10 kW under elevated thermal input conditions.

2. METHOD

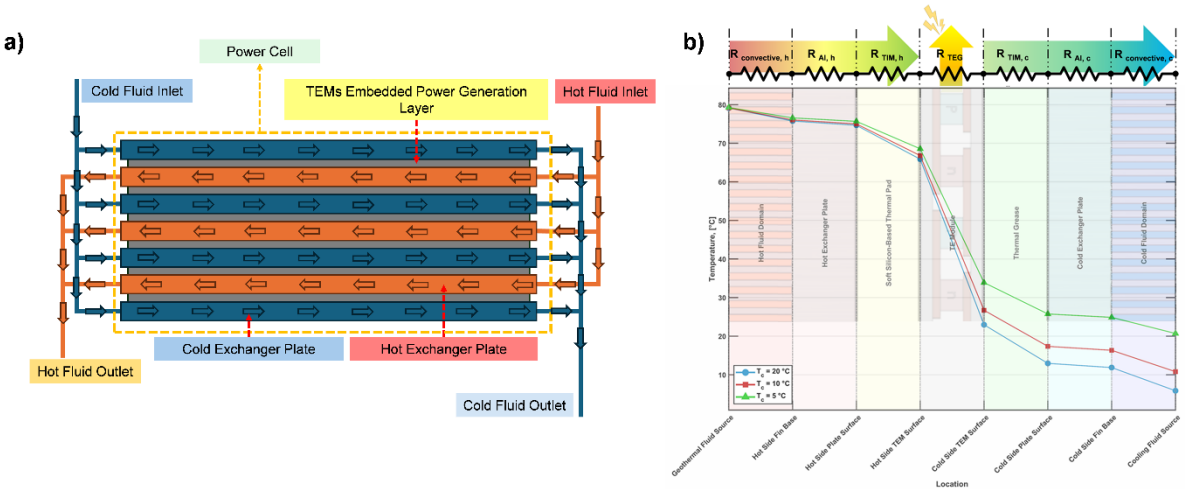

Figure 1: System configuration and operating principle of the thermoelectric geothermal power cell. (a) Counter-current plate type heat exchanger architecture with an embedded thermoelectric power generation layer, indicating hot and cold fluid inlets, outlets, and internal flow directions. (b) One-dimensional cross plane thermal resistance network with an example temperature distribution across the full stack at a 90 °C hot fluid inlet with a matched flow rate of 10 GPM, including convective boundaries, exchanger plates, and interconnect layers, and the effective power generation region under different cold-side conditions.

2.1 General Concept and System Schematic

The thermoelectric generator package, referred to as the power cell, integrates thermoelectric modules directly within a plate-type thermal exchange structure, enabling simultaneous heat transfer and electrical power generation within a single structural component. The system operates under a counter-current flow configuration, in which hot and cold fluid streams flow in opposite directions along the exchanger length, maintaining nearly uniform thermal boundary conditions across all thermoelectric modules. This arrangement suppresses the progressive decay of temperature gradients characteristic of parallel-flow configurations, thereby reducing position dependent performance variations. The resulting thermal uniformity also promotes consistent internal electrical resistance among modules, simplifying impedance matching and stack level electrical control (Fig. 1a). Heat transfer within the power cell can be described using an equivalent thermal-resistance network (Fig. 1b), in which resistances arise from convective fluid domains, exchanger plates, substrate layers, metallization

interfaces, and the thermoelectric elements themselves. This network determines the effective temperature drop across the active materials and thus governs the attainable conversion efficiency and electrical power output.

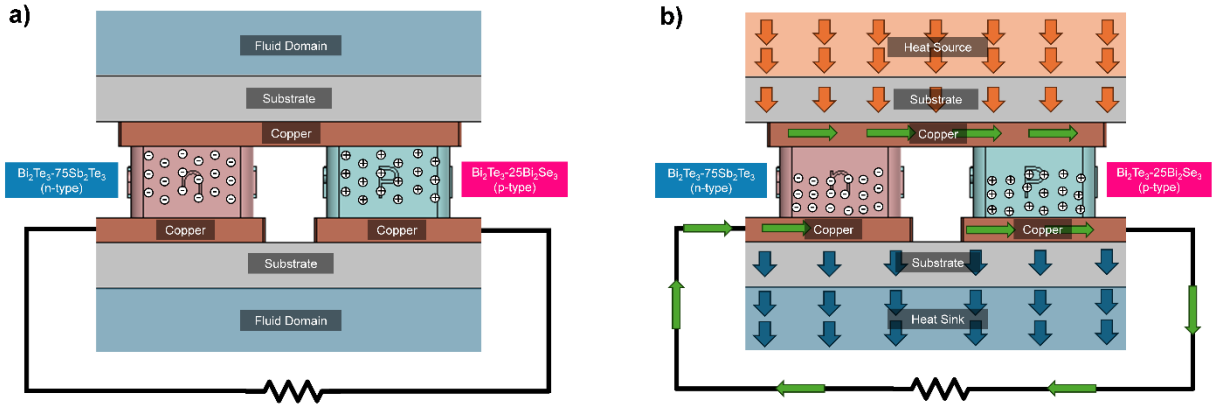

Figure 2: Cross-sectional architecture and thermal-electrical transport. (a) Cross sectional architecture of the thermoelectric module, including substrates, copper interconnects, and p-type and n-type legs. (b) Coupled thermal-electrical transport during operation, illustrating heat flow from source to sink and the associated electrical power generation.

Under isothermal equilibrium conditions, when the system reaches a uniform temperature, charge-carrier populations within the thermoelectric materials remain spatially balanced, resulting in no net electron or hole transport. Although thermal resistances exist at each material interface, including fluid domains, substrates, metallization layers, and the Bi_2Te_3 thermoelectric elements, the absence of a temperature gradient prevents the formation of an internal electric field or potential difference, corresponding to a non-operating state of the device (Fig. 2a). When a temperature gradient is imposed, electrical power generation is initiated through the Seebeck effect. Heat input at the hot side increases the energy of charge carriers, driving electrons toward the colder side and establishing a carrier concentration gradient across the thermoelectric material. This imbalance generates an internal electric field that induces directed charge transport. In p-type elements, hole transport dominates, whereas in n-type elements electron transport governs conduction. When the thermoelectric elements are connected through an external circuit, the resulting carrier flow produces a direct current output, enabling conversion of thermal energy into electrical power (Fig. 2b). Appropriate heat-sink design further sustains this process by maintaining large temperature gradients across the active thermoelectric materials.

2.2 Reduced Scale Experimental Testing Flow Loop

A reduced scale experimental platform was developed to enable controlled validation of thermoelectric power cell performance under representative thermal and hydraulic boundary conditions while minimizing overall system complexity. The integrated laboratory scale test platform shown in Fig. 3a allows controlled, repeatable, and independently verifiable characterization of thermoelectric power generation under geothermal relevant and industrial operating conditions. In contrast to small scale thermoelectric module tests that rely on cartridge heated plates to impose fixed temperature boundaries, the present flow loop based platform couples fluid thermal transport, solid conduction, and electrical power generation within a closed loop framework. This system level integration is essential for resolving performance metrics that depend sensitively on flow rate, inlet temperature stability, and parasitic heat losses at the power cell level.

A key feature of the testing platform is the decoupling of the hot side thermal supply loop from the cold side heat rejection loop. Independent storage tanks, circulation pumps, and flow control elements allow each loop to be operated under matched or deliberately asymmetric conditions. This configuration enables systematic investigation of flow rate dependent heat transfer coefficients, thermal resistance partitioning across the thermoelectric stack, and transient thermal responses to step changes in either heat source or heat sink conditions. The platform therefore supports both steady-state performance mapping and dynamic testing scenarios relevant to fluctuating geothermal flow environments.

The hot side thermal storage and circulation lines function as a controlled thermal reservoir, effectively acting as a thermal battery that stores thermal energy prior to the conversion process (Fig. 3b). By incorporating a large thermal mass, internal recirculation pathways, and multilayer insulation, the system suppresses short term temperature fluctuations arising from heater control dynamics or pump operation. This thermal buffering ensures that variations in electrical output can be attributed to changes in operating parameters rather than uncontrolled thermal noise. In addition, the inclusion of bypass

lines enables rapid adjustment of the effective thermal input without interrupting system operation, which is particularly valuable for parametric sweeps and repeatability studies.

The flow loop supports two distinct operating modes: a recirculation mode and a single pass mode. In the recirculation mode, the 2-way diverting valves shown in Fig. 3b and Fig. 3d route the working fluid back to the corresponding hot or cold reservoir, allowing the hot reservoir to be gradually depleted while transferring heat to the cold reservoir. This configuration enables both reservoirs and the overall platform, to progressively approach an isothermal state during flow testing, facilitating slow, wide range performance sweep evaluation. In the single pass mode, the flow is redirected through dedicated pathways to individual flow rate measurement storage tanks for the hot and cold loops, enabling precise characterization of flow rate and power generation without perturbing upstream thermal conditions.

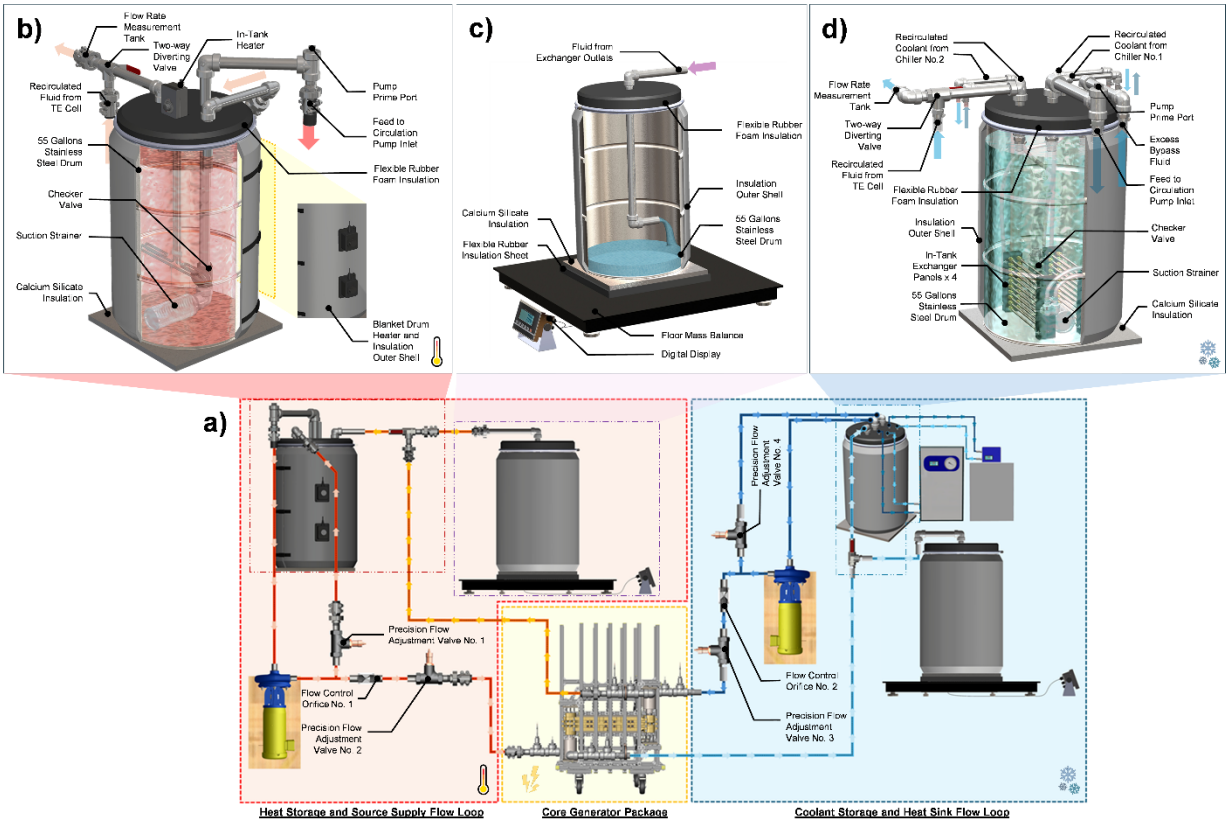

Figure 3: Integrated laboratory scale power cell testing platform and flow loop. (a) Schematic of the complete experimental system, including the heat storage and source supply loop, the core thermoelectric power cell package, the coolant storage and heat sink loop, illustrating fluid routing, flow control, and instrumentation. (b) Hot side thermal storage and circulation module incorporating the heating element, thermal insulation layers, and recirculation and bypass pathways. (c) Flow rate monitoring tank used for direct flow rate measurement based on mass change over time, enabling independent validation of volumetric flow rate through gravimetric measurement. (d) Cold side coolant circulation and heat rejection module with matched flow control, recirculation lines, and integrated instrumentation for steady state and transient testing.

The working fluid in the hot reservoir is heated using electric immersion heaters, while the cold reservoir is cooled through an in-tank tubular heat exchanger connected to two external chillers (Fig. 3d). The chillers circulate a solution composed of 90% propylene glycol and 10% distilled water to continuously extract heat from the cold reservoir. Heating the hot water reservoir from room temperature to approximately 95-98 °C requires ~6.8 h using a total installed heating power of 10.0 kW, provided by an 8.4 kW immersion heater and a 1.6 kW blanket-type drum heater. Under these conditions, the maximum inlet temperature delivered to the power cell reaches approximately 70-85 °C. Although alternative high temperature heat transfer fluids, such as Dowtherm A, could be employed to achieve higher inlet temperatures, institutional safety regulations precluded their use in the present study. By comparison, the two chillers consume a combined electrical power of 1.05 kW and require ~8.14 h to cool the cold water reservoir from room temperature to 0-2 °C.

Accurate flow characterization represents another critical aspect of experimental design. A gravimetric flow monitoring tank is employed to provide direct, physics-based validation of the volumetric flow rate based on measured mass change over time. The mass variation is video recorded and subsequently processed using a custom MATLAB-based image recognition pipeline to extract flow rates autonomously and with high accuracy. This approach avoids sole reliance on manufacturer-calibrated flow sensors, which can exhibit non-negligible errors under elevated temperatures or when non-Newtonian working fluids are employed.

To evaluate system stability under fault tolerant operating conditions, one thermoelectric matrix was deliberately omitted from the nominal fourth generation layer. This modification reduced the assembly from the standard 16 matrices configuration to 15 matrices, comprising a total of 170 thermoelectric modules (compared with the nominal 4 × 46 module configuration). The reduced stack was arranged between three cold side and two hot side heat exchanger plates. An adjustable external mechanical clamping system was also employed to preserve structural integrity under potential mechanical failure scenarios. In addition, a calcium silicate board was incorporated as a thermal isolation layer between the test fixture and the power cell to minimize parasitic heat losses and isolate boundary effects.

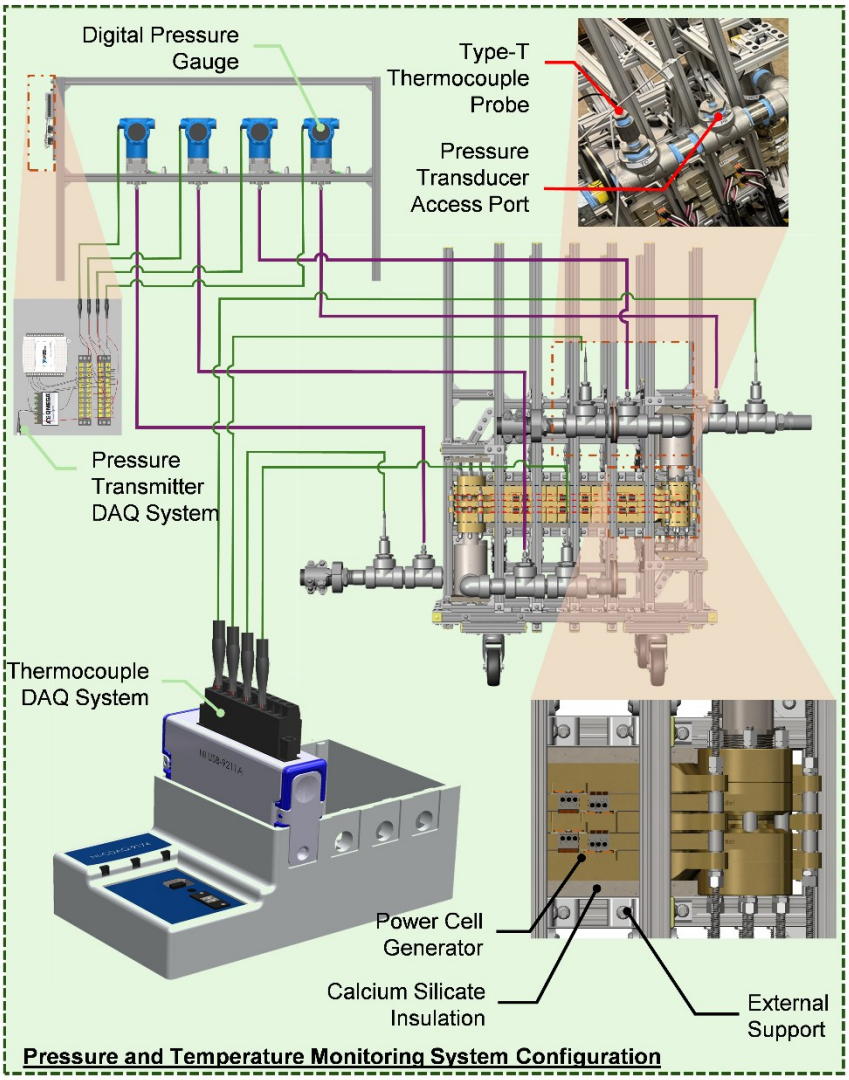

Figure 4: Schematic of the data acquisition setup for power cell testing.

2.3 Generator Performance and Electrical Testing Configuration

Temperature, pressure, and electrical signals are continuously recorded to characterize power cell performance under laboratory testing conditions. The electrical configuration explicitly separates power routing paths, circuit protection elements, and data acquisition channels, enabling reliable operation together with high resolution diagnostics at both the panel and system levels. While the overall system architecture is designed to support high voltage output configurations

suitable for integration with downstream power electronics and grid interfaces, all thermoelectric generation layers are electrically connected in parallel during laboratory testing. This configuration limits the output voltage to below 60 V, ensuring compliance with human safety requirements during experimental validation (Fig. 4).

Pressure monitoring and flow-related instrumentation are integrated into the same data acquisition network as the thermoelectric measurements, allowing thermal-hydraulic conditions to be recorded simultaneously with electrical performance. This unified acquisition strategy enables identification of coupled effects, such as variations in electrical output driven by flow dependent heat transfer. By treating pressure, temperature, and electrical output as a single coupled dataset, the platform avoids fragmented interpretation that can arise when subsystems are monitored independently.

2.4 Testing procedure and Infrared Imaging

To prepare for each experiment, the hot and cold water reservoirs were filled to full capacity, and the circulation pumps were primed before startup. Fluids in the hot and cold side loops were then continuously circulated through the power cell to purge trapped air bubbles from the pipelines until all residual air was either displaced or dissolved into the aqueous phase. Once complete saturation of the loops was achieved, the pumps and flow control valves were temporarily shut off to allow the hot and cold reservoirs to reach their target temperatures under static conditions. Throughout the heating and cooling phases, the electrical circuit breakers remained disengaged and were only activated during the final injection and power generation stage to ensure controlled startup and safe operation. Prior to initiating each test, both the hot and cold side circulation loops were reprimed to ensure complete saturation of the fluid loops with no trapped air gaps. To initiate testing, the electrical circuits and data acquisition systems were activated, after which the cold fluid loop was circulated first until the power cell reached an isothermal state, followed by starting circulation of the hot fluid loop. This staged injection sequence prevents overheating of internal electronics and components by ensuring adequate cooling before thermal loading. During testing, hot and cold working fluids were delivered at constant flow rates, circulated through the generator, and returned to their respective reservoirs depending on the operating mode (Fig. 5).

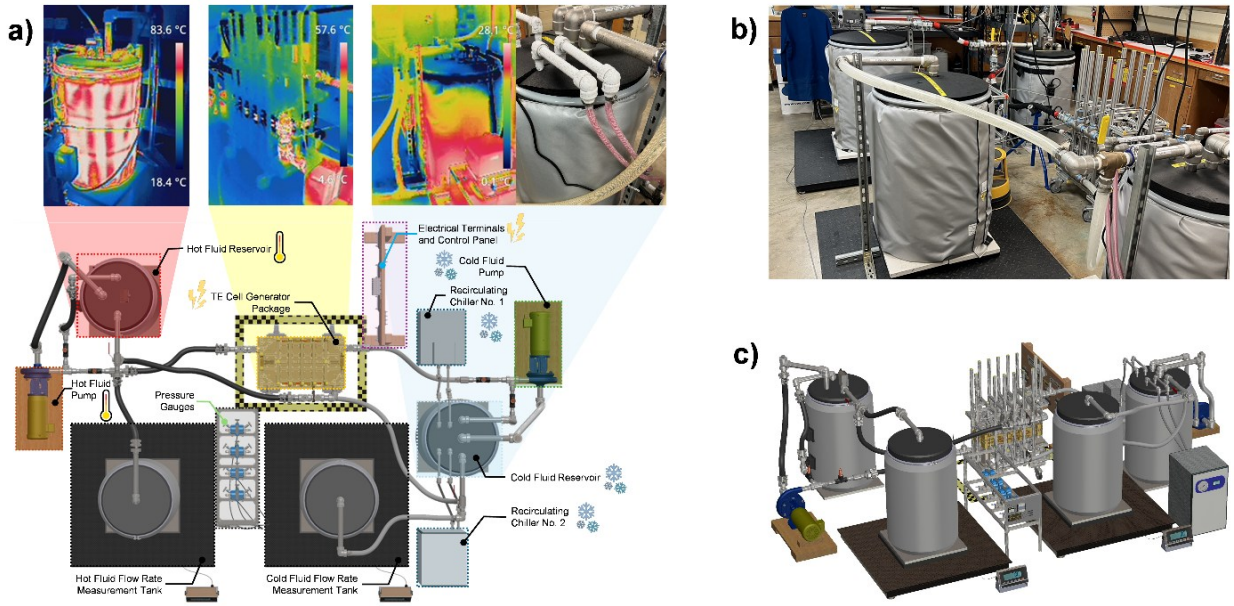

Figure 5: Integrated power cell test configuration and thermal characterization under operating conditions. (a) System level schematic of the thermoelectric power cell experimental setup, together with representative infrared thermal images highlighting temperature distributions across key components during active operation. (b) Photograph of the laboratory scale thermoelectric power cell testing platform. (c) Three-dimensional rendering of the complete experimental assembly, showing the relative placement of thermal storage units, the thermoelectric generator package, flow control components, and measurement systems.

Infrared thermal images shown in Fig. 5a illustrate representative temperature distributions across the hot and cold fluid reservoirs, the power cell package, and the associated piping during single pass measurement mode. These measurements confirm that the thermal gradients driving power generation are established primarily across the intended heat transfer interfaces, rather than being dominated by parasitic heat losses through structural components or external tubing. The observed temperature stratification within the hot and code side reservoir further validates the role of the thermal storage

and sink in stabilizing inlet conditions, while the relatively uniform surface temperature of the exchanger plate indicates effective heat spreading and controlled thermal contact across the active generation area.

2.5 Reduced Scale Mk III Circulation Mode Testing Results

Under continuous circulation mode testing, the flow rate was set to 10 GPM per plate, corresponding to the maximum operating flow rate of the experimental platform. Lower flow rates can be readily employed as required. Three cold side plates were operated in parallel, yielding a total cold side flow rate of 30 GPM, while the hot side loop employed two hot plates with matched per plate flow control. Thermoelectric performance under this configuration serves as a representative test case, providing insight into the coupled thermal-electrical dynamics governing the power cell generation profile. During the experiment, the heating element was kept active to slow the rate of thermal depletion of the hot side reservoir. Over the full transient window (0-14,000 s), the system transitions from startup toward a quasi-steady thermal state as the hot side thermal reservoir is progressively depleted. During this period, the hot side inlet temperature decreases from approximately 87 °C to 61 °C, while the cold side inlet temperature increases from approximately 7 °C to 58 °C, indicating a gradual reduction in the usable temperature difference across the thermoelectric stack. The system consequently approaches thermal equilibrium, beyond which sustained power generation becomes negligible.

The electrical response closely follows this thermal evolution, demonstrating strong thermal electrical coupling. The output current decays from ~12 A to ~0.4 A (Fig. 6a), while the terminal voltage decreases from ~18 VDC to ~0.6 VDC (Fig. 6b) as the system level temperature difference diminishes. Correspondingly, the electrical power output drops sharply from an initial peak exceeding 200 W (approximately ~220 W) to near-zero values over the transient period (Fig. 6d), highlighting the strong dependence of thermoelectric conversion performance on the available thermal driving force. The effective electrical resistance initially undergoes tuning toward a load-matched condition, consistent with near-optimal power extraction during the early stage of testing (Fig. 6c). However, if the external load resistance is held fixed, continued thermal evolution leads to a progressive departure from maximum power point operation and reduced electrical conversion effectiveness.

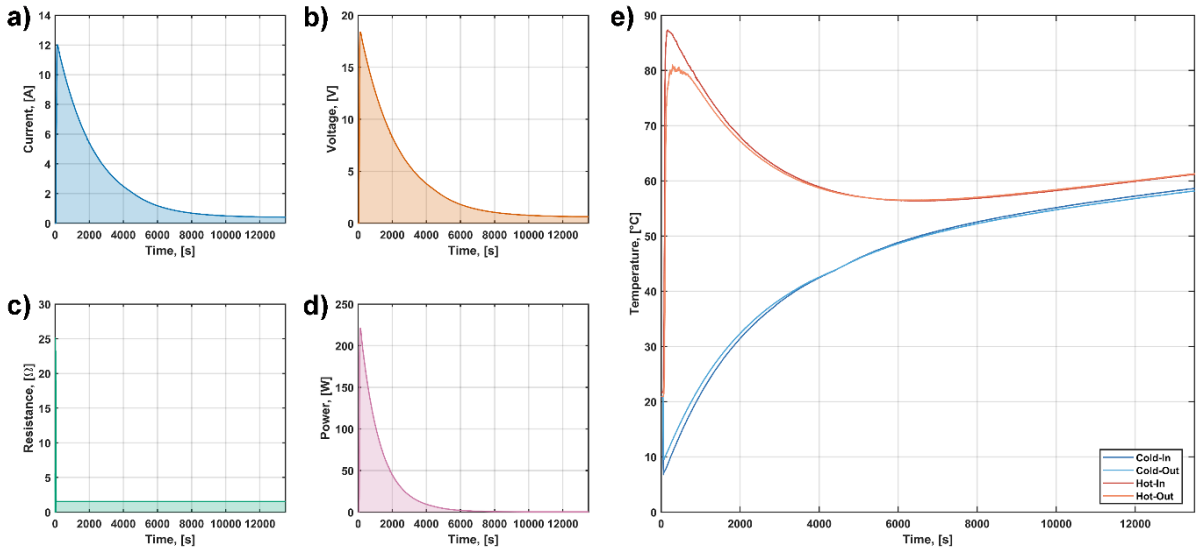

Figure 6: Time evolution of the power cell performance under continuous circulation mode testing. (a) Output current decay, (b) terminal voltage decay, (c) effective electrical resistance and initial load matching, and (d) electrical power output as a function of time. (e) Transient temperature response of the hot and cold side fluid inlets and outlets, illustrating the coupled thermal-electrical dynamics during system cooldown.

The circulation mode configuration is also representative of a thermally cascaded arrangement of power cells along the flow direction, in which each successive stage operates under a progressively reduced available temperature head. Although the modules are thermally connected in series along the fluid flow path, the measured electrical performance reflects the aggregate response of all modules operating under spatially varying thermal boundary conditions.

3. RESULTS

3.1 Reduced Scale Mk III Single Pass Mode and Impedance Matching Results

The transient electrical and thermal response under the single pass flow configuration demonstrates dynamic resistance matching for maximizing power extraction from the thermoelectric power cell. In contrast to continuous circulation mode, this operating condition is designed to characterize load-impedance matching behavior and identify optimal operating points under relatively stable and well-controlled thermal boundary conditions. The resulting load trajectory provides a practical reference and an initial estimate for the maximum power point tracking (MPPT) control strategy implemented on the electrical control side.

For the representative test case operated at 10 GPM per plate, the first ~70 s correspond to the experimental preparation stage, during which the data acquisition system is initialized, system diagnostics are checked, and the flow loops are primed. Following this phase, cold side fluid injection is initiated and is shortly followed by hot side fluid injection. Owing to the limited hot side reservoir capacity (~55 gallons), the total experiment duration is constrained to less than ~2 min for high flow rate test cases. The system initially operates under baseline thermal conditions, with the cold side reservoir temperature near ~8-10 °C and the hot side reservoir temperature at approximately ~75-78 °C. At approximately 75 s, the initiation of hot and cold side fluid injection induces a rapid thermal transient, driving the power cell to experience an increase in hot side inlet temperature from ~20 °C to ~78 °C within seconds, while the cold side inlet temperature decreases from room temperature to approximately ~7 °C (Fig. 7e). This sudden establishment of a large temperature gradient ($\Delta T \approx 71$ °C) initiates the thermoelectric energy conversion process. Beyond performance characterization, this rapid temperature excursion also serves as a structural integrity and long-term thermal stress screening test, enabling evaluation of system response under intense thermal cycling and thermal shock conditions across repeated experiments.

After the system approaches a relative thermal equilibrium at approximately 111 s, the impedance matching process is initiated. The first voltage ramp up is observed in Fig. 7b, where the effective open-circuit voltage reaches approximately ~39 VDC. During this stage, the external load resistance is dynamically adjusted from near zero to approximately 100 Ω (Fig. 7c), with finer resolution applied over the region of primary interest. Specifically, the load resistance is swept from 1-5 Ω using a 0.125 Ω step size, followed by coarser 10 Ω increments from 5 Ω to 100 Ω, after which the experiment is terminated.

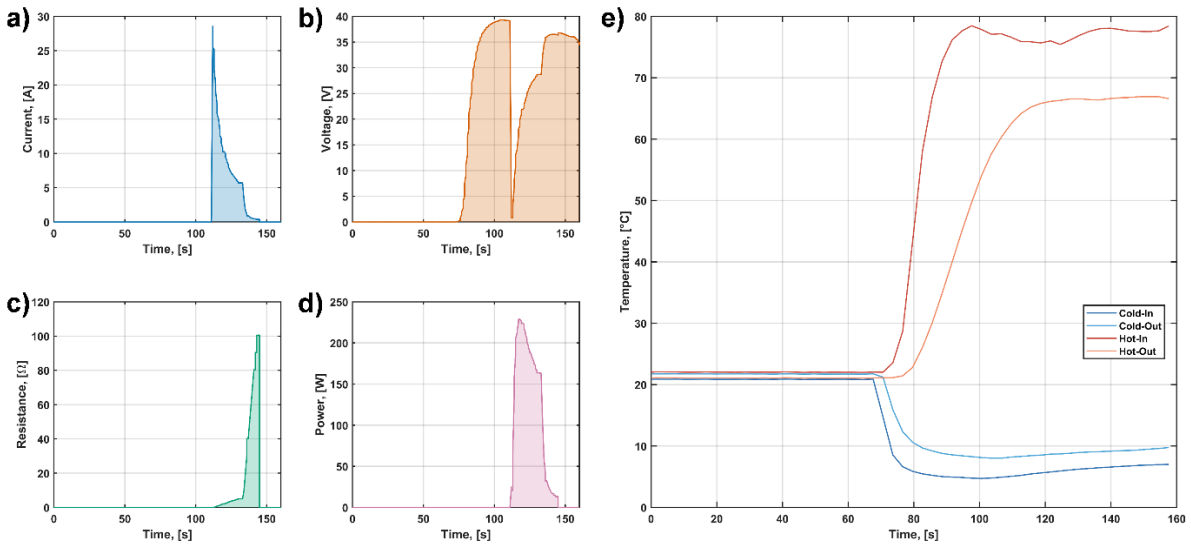

Figure 7: Time-resolved electrical and thermal response of the power cell under a single flow path configuration for resistance impedance matching. (a) Output current, (b) terminal voltage, (c) electrical resistance loading, and (d) electrical power output as functions of time. (e) Corresponding transient temperature evolution at the power cell hot and cold side inlets and outlets.

The electrical response indicates effective impedance matching throughout the thermal transient. The output current reaches a sharp peak of ~28.5 A as the maximum temperature difference is established (Fig. 7a), resulting in a peak electrical power output exceeding 220 W (approximately ~228 W; Fig. 7d). These results confirm the effectiveness of the single-pass, dynamically tuned impedance-matching strategy for capturing peak thermoelectric performance.

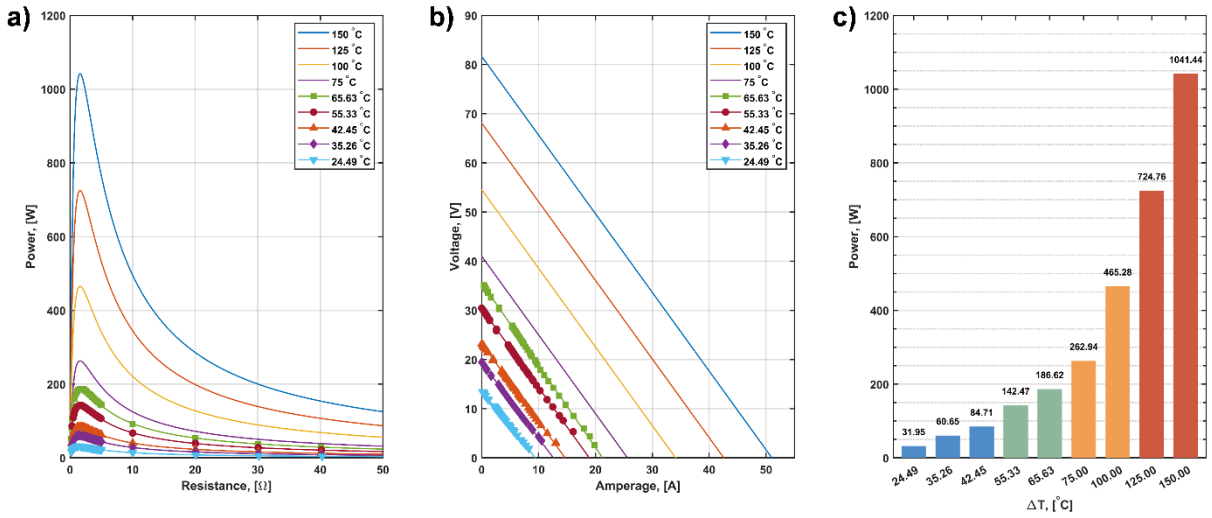

Figure 8: Electrical performance characteristics of the power cell under varying temperature gradients. (a) Electrical power output as a function of external load resistance for different temperature differences. (b) Voltage-current characteristics corresponding to the same operating conditions. (c) Maximum electrical power output as a function of temperature difference, illustrating the scaling of peak power with increasing thermal driving force.

3.2 Mk III System Performance Summary and Projection

At the experimental scale, a sustained temperature difference of 65-70 °C was successfully established across the power cell. Under these conditions, each power generation layer produced approximately 57 W, increasing to 63.75 W when fully populated with a 16-matrix configuration. The reduced power cell package delivered a total electrical output of 255 W, corresponding to output voltages of 28.5-30.4 VDC and currents of 8.4-8.9 A. Beyond instantaneous performance, the system exhibited stable electrical output over hundreds of thermal cycles during extended operation. Since completion of the Mk III prototype in September 2023, the power cell has been operated and tested for nearly two years without measurable degradation in power output or electrical characteristics, demonstrating long-term durability under thermally demanding conditions.

Fig. 8 summarizes the electrical performance of the thermoelectric power cell over a wide range of imposed temperature differences, including projected operation at elevated heat source temperatures. All measurements were conducted at fixed hot and cold side flow rates of 10 GPM per plate using a 15-matrix configuration. The power-resistance characteristics (Fig. 8a) exhibit the expected single peaked load power profiles, with well-defined maxima identifying the optimal load-matching condition at each temperature difference; at the highest evaluated condition (ΔT = 150 °C), the projected maximum power output exceeds 1 kW at an optimal load resistance of approximately 1.7 Ω. As ΔT increases, both the peak power and the corresponding optimal load resistance shift toward higher values, reflecting the combined effects of increased Seebeck voltage generation and temperature dependent charge transport processes that modify the effective internal resistance of the thermoelectric modules. Consistent with this behavior, the voltage-current characteristics (Fig. 8b) display linear V-I relationships, with the open-circuit voltage increasing from approximately 19.5 V at ΔT = 35.26 °C to 81.6 V at ΔT = 150 °C, while the short-circuit current exhibits a similar monotonic increase. These linear characteristics indicate stable internal electrical behavior with minimal parasitic losses and support straightforward series-parallel scaling toward industrial high-voltage DC standards (208-600 V). These trends are consolidated in Fig. 8c, which shows that the maximum power output increases from 31.95 W at ΔT = 24.69 °C to 1041.41 W at ΔT = 150 °C (1127 W when fully populated, corresponding to conversion efficiencies of ~0.34-2.94%), corresponding to more than a 30-fold enhancement across the evaluated range. This near-quadratic dependence of power on temperature difference (power $\propto \Delta T^n$, with $n \approx 1.94$) arises from the combined increase in Seebeck voltage and more effective utilization of the applied thermal driving force at higher temperature gradients. These trends underscore the importance of maintaining large, sustained temperature differences and implementing dynamic load-control strategies to preserve optimal impedance matching as thermal boundary conditions evolve.

4. UPSCALED FIELD UNIT (MK IV) AND FIELD-SCALE GRID DEPLOYMENT

4.1 Mk IV Power Cell

The Mk IV power cell retains the established flow configuration of the Mk III system to preserve the thermal-hydraulic advantages demonstrated in earlier generations, while introducing targeted modifications to the internal architecture that enable operation at substantially higher temperatures, up to 225 °C, and under harsher field conditions (Fig. 9). These upgrades include reinforced protective covers and improved sealing strategies to enhance resistance to moisture ingress and environmental exposure. The Mk IV platform also incorporates a newly designed thermoelectric module optimized for high temperature operation and mechanical robustness; the initial unit comprises 16 power generation layers containing a total of 736 thermoelectric modules.

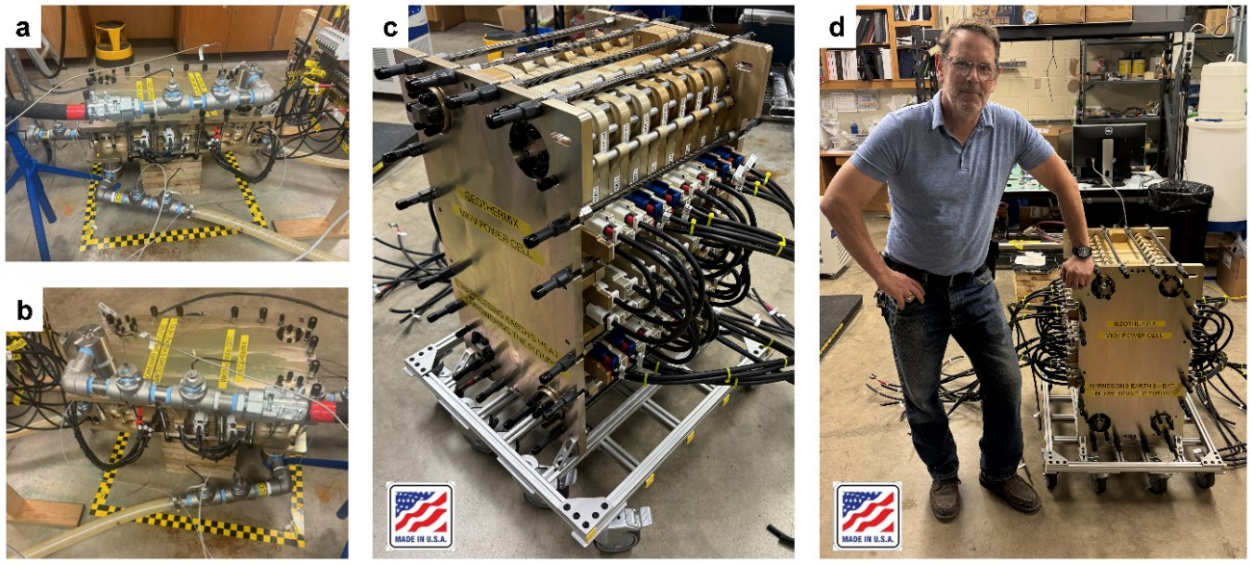

Figure 9: Photographs of the Mk IV power cell designed for elevated temperature operation. (a), (b), Side and top views of a 5 plates, 4 generation layers stacked Mk IV unit during flow testing. (c), (d), Fully assembled Mk IV 17 plates, 16 generation layers power cell mounted on a mobile structural frame, highlighting the overall system footprint and modular architecture.

The electrical scaling behavior of the Mk IV thermoelectric power cell under varying thermal conditions is shown in Fig. 10. Experimental results are obtained up to $\Delta T \approx 65$ °C at the designed flow rate of 10 GPM per plate using a 5-plate stack, with higher ΔT performance extrapolated based on the validated electrical scaling behavior. The output voltage increases approximately linearly with ΔT and follows an identical trend for the single-layer, 4-layer laboratory unit, and 16-layer field scale configuration, demonstrating that voltage remains unchanged under idealized parallel electrical integration, which aggregates current while preserving the voltage level. Under a fully parallel configuration, the output current is projected to reach 103.7 A at $\Delta T = 225$ °C, highlighting practical constraints associated with pure parallel architectures, including the requirement for oversized busbars and specialized high current interconnects; these considerations motivate the adoption of optimized series-parallel electrical configurations for practical grid level implementations. The combined voltage and current scaling leads to a rapid increase in electrical power output (Fig. 10c), with power rising from the sub-kilowatt regime at low ΔT to approximately 2 kW at $\Delta T \approx 100$ °C, ~4.6 kW at $\Delta T \approx 150$ °C, and exceeding 10 kW as ΔT approaches 220 °C for the fully populated 16-layer field configuration.

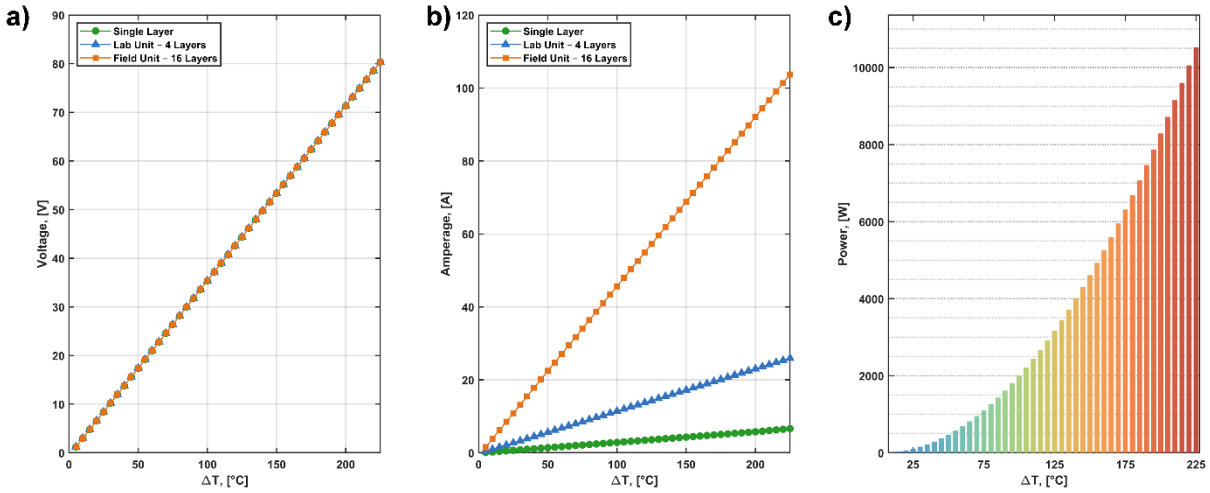

Figure 10: Electrical performance of the Mk IV power cell as a function of temperature difference. (a) Output voltage for a single generation layer, a 4-layer laboratory unit, and a 16-layer field scale unit with a parallel electrical configuration. (b) Output current for the same configurations. (c) Electrical power output of the fully populated field-scale configuration.

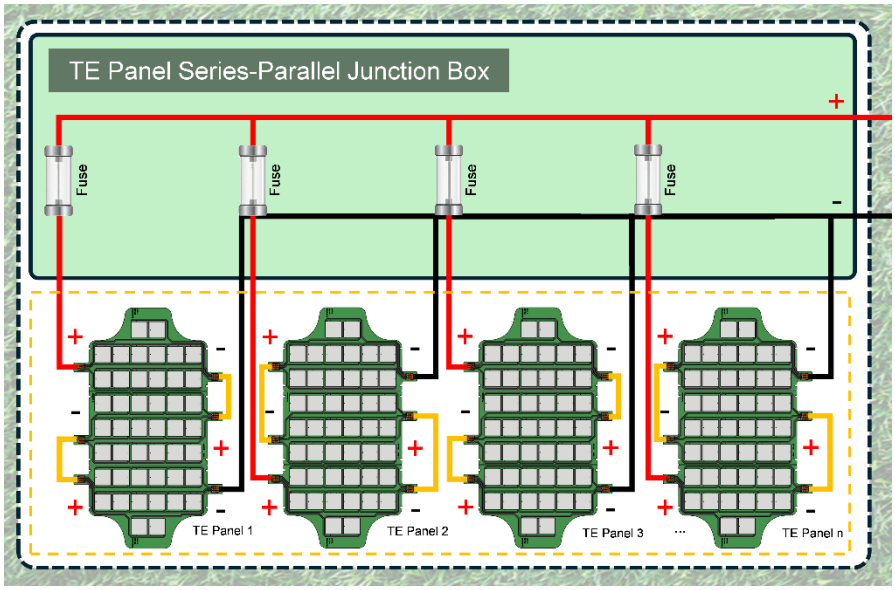

Figure 11: Series-parallel electrical interconnection of thermoelectric panels with integrated junction protection

4.2 Field Scale Grid Deployment Strategy

The grid level integration represents a key enabler for practical thermoelectric waste heat recovery, bridging the gap between laboratory scale device characterization and field deployable power generation systems. The architecture accommodates both islanded operation for remote applications and grid-tied configurations for industrial facilities, with intelligent power management enabling optimal energy harvesting under real-world operating conditions where thermal input varies dynamically.

The thermoelectric panels are configured in a hybrid series-parallel junction box, in which individual matrices within each panel are connected in series to increase voltage, while multiple panels are interconnected through a combined series-parallel scheme to match the electrical requirements of downstream power-conditioning components, including DC-AC converters and control electronics (Fig. 11). This configuration balances high voltage output with adequate current delivery, overcoming the limitations of purely series connected designs for practical grid-scale operation.

4.3 Power Cell Integration in Enhanced Geothermal Systems (EGS)

The integration of power cells within an enhanced EGS provides a system level strategy for reducing parasitic loads by harvesting energy directly from existing surface facility heat transfer pathways (Fig. 12a). Power cells can be flexibly deployed at multiple locations along the surface facility process train, including upstream production exchanger bays, intermediate flash fluid separation stages, and downstream cooling tower or turbine exhaust pathways, enabling broad compatibility with existing geothermal plant infrastructure.

The surface facility layout shown in Fig. 12b illustrates a representative implementation in which power cells are integrated into the exchanger bay section of the plant. Hot geothermal fluid extracted from the production well is routed through a cascaded array of power cells arranged in series, allowing progressive thermal energy extraction while preserving the highest available thermal head for power conversion at each stage (Fig. 13a). The number of power cell stages is determined by the geothermal fluid thermal mass flow rate and the marginal economic benefit of continued heat recovery, such that thermoelectric extraction is terminated once the remaining temperature head no longer justifies further conversion.

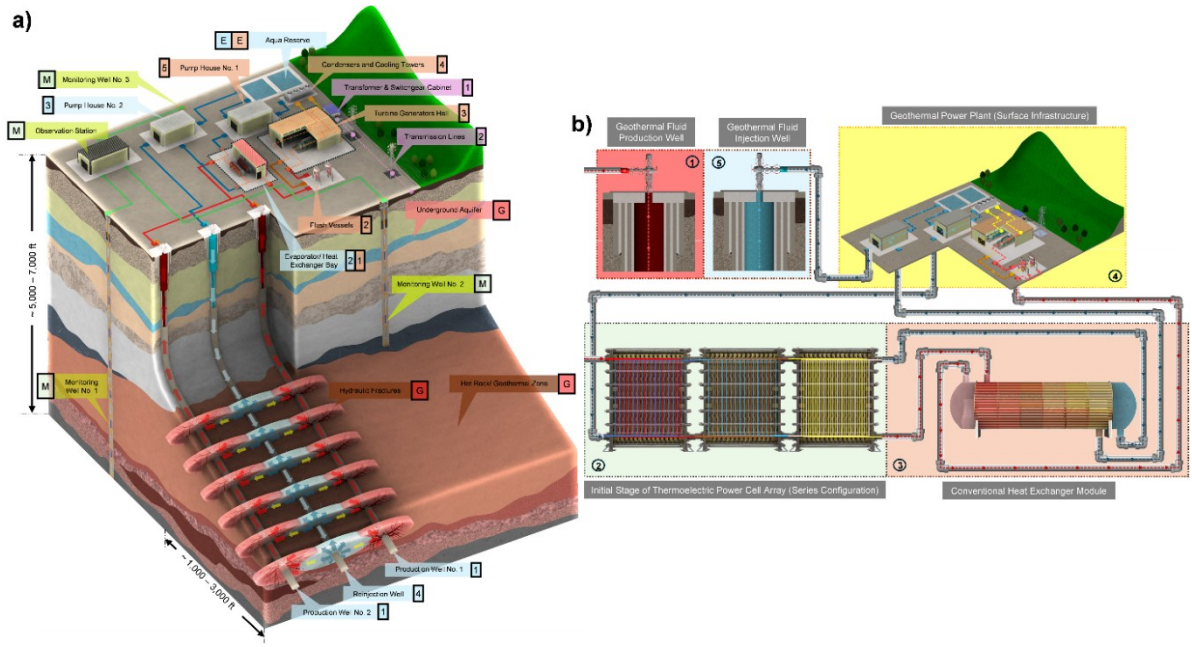

Figure 12: System level integration of power cells in a geothermal power plant. (a) Schematic of subsurface and surface geothermal infrastructure, including production and injection wells, fracture network, and surface facilities. (b) Coupling of geothermal fluid circulation with a thermoelectric power cell array and a conventional heat exchanger module, illustrating the initial series configured thermoelectric stage and its integration with existing plant infrastructure.

Following thermoelectric conversion, the partially cooled geothermal fluid enters a conventional heat exchanger module positioned downstream of the power cell array. This section performs final stage heat recovery prior to downstream power plant processes, capturing residual thermal energy that would otherwise remain unutilized. In this configuration, the power cell does not replace the conventional heat exchanger outright; instead, it functions as a distributed, energy harvesting heat exchange stage while maintaining full compatibility with established geothermal plant infrastructure. The thermally conditioned fluid existing the exchanger then serves as the standard feed stream for the remaining energy conversion processes within the enhanced geothermal system power plant.

For end of process cooling, the power cell array can alternatively be arranged in a unit wise counter-current configuration with coolant reintroduced at each stage (Fig. 13b). This configuration maintains a consistently higher temperature difference across each unit by effectively resetting the coolant injection temperature at every stage. The modular power cell grid shown in Fig. 13c illustrates how multiple power cell arrays can be combined to form a scalable power harvesting grid. The representative 3 × 6 grid configuration highlights the flexibility to independently adjust array size and staging strategy, enabling deployment tailored to available thermal resources and power demand. This modularity allows thermoelectric power cell grids to be scaled from multi-kilowatt systems to several hundred kilowatts, providing a pathway to enhance the efficiency of existing geothermal plants and industrial processes operating over a wide temperature range of 50-225 °C, where typical conversion efficiencies fall in the range of 0.83-3.88%. In addition, the power cell grid supports system level

health monitoring, enabling the thermoelectric array to function as a diagnostic layer for geothermal system performance or as an indicator of end of process thermal emissions in industrial applications.

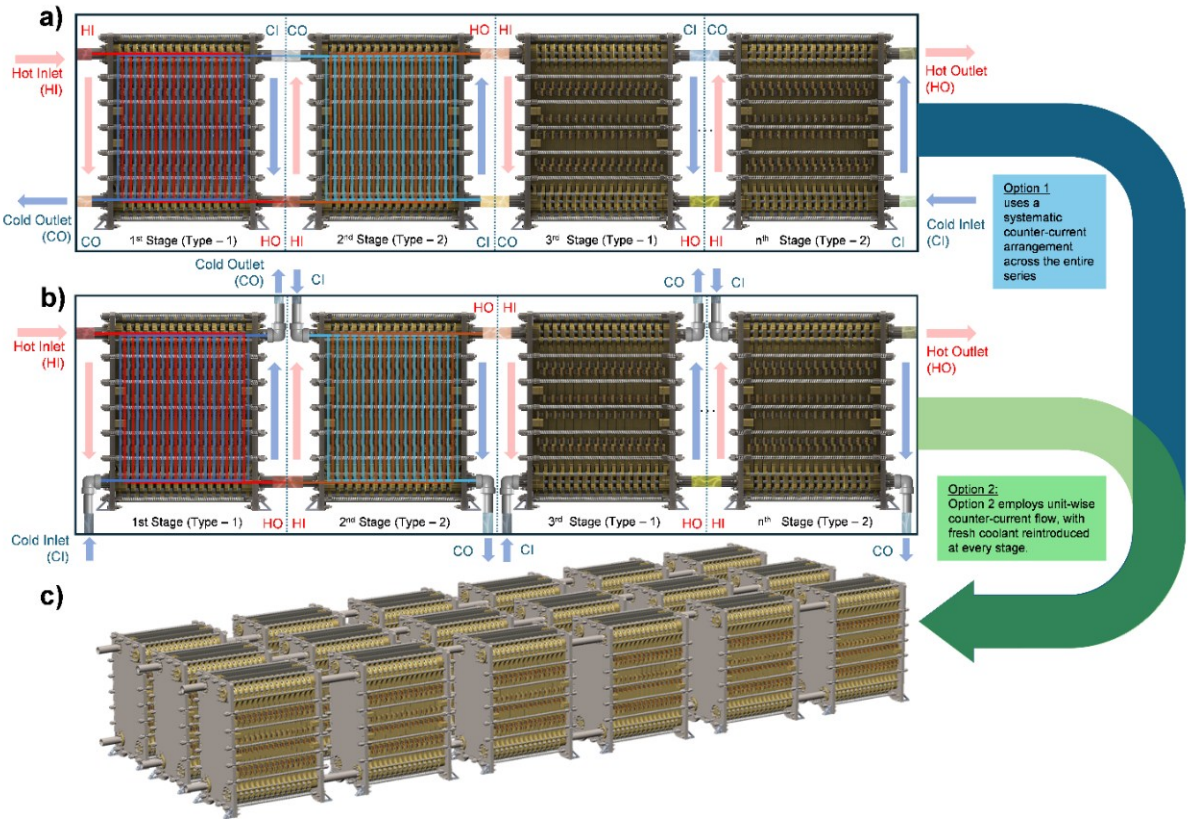

Figure 13: Counter-current flow configurations for a cascaded power cell grid. (a) System wide counter-current flow across the entire series of stages. (b) Unit wise counter0current flow with coolant reintroduced at each stage. (c) Example thermoelectric power cell grid in a 3 × 6 configuration.

5. CONCLUDING REMARKS

In summary, this study demonstrates a scalable and field deployable thermoelectric generator for geothermal and industrial waste heat recovery, capable of directly converting low to medium temperature heat streams (50-225 °C) into electricity via solid state Seebeck conversion. Highly integrated thermoelectric generation layers based on Bi_2Te_3 modules are embedded within rigid or rigid-flex integrated circuit boards and coupled to a counter current, plate type heat exchanger architecture. This co-designed system unifies heat transfer and power generation within a compact, mechanically simple package that is compatible with mass manufacturing and real-world deployment.

Laboratory testing under geothermal relevant flow conditions validated both electrical performance and operational durability. A reduced 4-module stack produced ~228 W at a temperature difference of ΔT = 71 °C, corresponding to a projected output of approximately 1.02 kW when scaled to a full 16-module configuration. Across the tested operating envelope, the maximum electrical power exhibited an approximately quadratic dependence on the applied temperature difference, supporting projections toward multi-kilowatt unit output as larger thermal gradients become available in field conditions. The measured thermal to electrical conversion efficiency varied with temperature gradient and system configuration, ranging from approximately 0.34% to 2.94% over the 25-150 °C operating range.

The later Mk IV upscaled architecture extends this platform to elevated operating temperatures of up to 225 °C through improved sealing, next generation power electronics, reinforced structural protection, upgraded heat transfer surfaces, and a high temperature thermal interface system. Under these conditions, the design projects power generation capacities exceeding ~10 kW, with conversion efficiencies in the range of approximately 0.83-3.88%. When integrated with power conditioning and grid interfacing strategies incorporating protection, monitoring, and maximum power point tracking for dynamic impedance matching, these advances establish a practical pathway for deploying thermoelectric power cells in geothermal surface facilities, including heat exchanger bays, separator stages, turbine exhaust streams, and heat rejection processes. The same architecture is readily transferable to other industrial waste heat recovery applications. Performance

assessments and life cycle analyses of both laboratory scale and field oriented prototypes further indicate the feasibility of continuous 24/7 operation, with a levelized cost of electricity comparable to that of conventional solar technologies.

ACKNOWLEDGEMENTS

Work carried out at the University of Texas at Austin was supported in part by the U.S. Department of Energy since 2022.We would like to thank Geothermix as well as the PGE Machine Shop at the University of Texas at Austin. We particularly acknowledge Daryl Nygaard for his assistance during system installation and development. Copyright reserved.

REFERENCES

Bell, L. E. (2008). Cooling, Heating, Generating Power, and Recovering Waste Heat with Thermoelectric Systems. *Science*, *321*(5895), 1457–1461. https://doi.org/10.1126/science.1158899

Bertani, R. (2015). Geothermal Power Generation in the World - 2010–2015 Update Report. In *Proceedings World Geothermal Congress*.

DiPippo, R. (2016). Geothermal Power Plants Principles Applications Case Studies and Environmental Impact. In *Geothermal Power Plants Principles Applications Case Studies and Environmental Impact* (4th ed., pp. 3–18). Elsevier. https://doi.org/10.1016/b978-0-08-100879-9.00001-x

Hao, F., Qiu, P., Tang, Y., Bai, S., Xing, T., Chu, H. S., Zhang, Q., Lu, P., Zhang, T., Ren, D., Chen, J., Shi, X., & Chen, L. (2016). High efficiency Bi2Te3-based materials and devices for thermoelectric power generation between 100 and 300 °c. *Energy and Environmental Science*, *9*(10), 3120–3127. https://doi.org/10.1039/c6ee02017h

Li, K., Garrison, G., Zhu, Y., Moore, M., Liu, C., Hepper, J., Bandt, L., Horne, R., & Petty, S. (2021). Thermoelectric power generator: Field test at Bottle Rock geothermal power plant. *Journal of Power Sources*, *485*. https://doi.org/10.1016/j.jpowsour.2020.229266

Liu, X., Cai, D., Ukwuoma, C. C., Huang, Q., & Bamisile, O. (2024). A survey of geothermal power generation combined with renewable energy for low carbon emissions. *Clean Energy*, *8*(3), 138–146. https://doi.org/10.1093/ce/zkad090

Lund, J. W., Huttrer, G. W., & Toth, A. N. (2022). Characteristics and trends in geothermal development and use, 1995 to 2020. *Geothermics*, *105*. https://doi.org/10.1016/j.geothermics.2022.102522

Luo, D., Yu, Y., Yan, Y., Chen, W. H., & Cao, B. (2024). Increasing power densities in a thermoelectric generator by stacking and incorporating dual heat pipes. *Device*, *2*(8). https://doi.org/10.1016/j.device.2024.100435

Nath, F., Mahmood, M. N., Ofosu, E., & Khanal, A. (2024). Enhanced geothermal systems: A critical review of recent advancements and future potential for clean energy production. In *Geoenergy Science and Engineering* (Vol. 243). Elsevier B.V. https://doi.org/10.1016/j.geoen.2024.213370

Rybach, L., & Kohl, T. (2004). Energy, Waste, and the Environment: a Geochemical Perspective. In *Geological Society* (Vol. 236). Special Publications. https://www.lyellcollection.org

Wang, L., Li, K., Zhu, Y., Hao, W., Zhang, F., Shi, Y., Wang, Y., & Yang, S. (2025). Coaxial geothermal wellbore thermoelectric power generation system: design, experimentation, and performance analysis. *Applied Thermal Engineering*, *271*. https://doi.org/10.1016/j.applthermaleng.2025.126349

Xie, H., Gao, T., Long, X., Sun, L., Wang, J., Xia, E., Li, S., Li, B., Li, C., Gao, M., & Mo, Z. (2023). Design and performance of a modular 1 kilowatt-level thermoelectric generator for geothermal application at medium-low temperature. *Energy Conversion and Management*, *298*. https://doi.org/10.1016/j.enconman.2023.117782

Zarrouk, S. J., & Moon, H. (2014). Efficiency of geothermal power plants: A worldwide review. In *Geothermics* (Vol. 51, pp. 142–153). https://doi.org/10.1016/j.geothermics.2013.11.001

Zhang, Q., Deng, K., Wilkens, L., Reith, H., & Nielsch, K. (2022). Micro-thermoelectric devices. *Nature Electronics*, *5*(6), 333–347. https://doi.org/10.1038/s41928-022-00776-0

Zhang, X., He, M., & Zhang, Y. (2012). A review of research on the Kalina cycle. In *Renewable and Sustainable Energy Reviews* (Vol. 16, Issue 7, pp. 5309–5318). https://doi.org/10.1016/j.rser.2012.05.040